

The 15 January 2022 Hunga Tonga eruption history as inferred from ionospheric observations

E. Astafyeva¹, B. Maletckii¹, T. D. Mikesell², E. Munaibari³, M. Ravanelli¹, P. Coisson¹, F. Manta³, L. Rolland³

1 – *Université Paris Cité, Institut de physique du globe de Paris (IPGP), 35-39 Rue Hélène Brion, 75013 Paris, France, astafyeva@ipgp.fr*

2 – *Norwegian Geotechnical Institute, Natural Hazards, Oslo, Norway*

3 – *Université Côte d'Azur, Observatoire de la Côte d'Azur, CNRS, IRD, Géoazur, 250 rue Albert Einstein, Sophia Antipolis 06560 Valbonne, France.*

Keypoints:

- Ionospheric TEC data reveal that the 15 January 2022 Hunga Tonga volcanic eruption involved at least 5 large explosions between 4 and 5UT
- From TEC observations, we estimate the onset time to be 04:05:54UT and the main explosion energy release of 9 to 37 Megatons TNT equivalent
- The eruption-driven shock wave caused an unprecedentedly strong and long-lasting depletion in the ionosphere

Abstract

On 15 January 2022, the Hunga Tonga-Hunga Ha'apai submarine volcano erupted violently and triggered a giant atmospheric shock wave and tsunami. The exact mechanism of this extraordinary eruptive event, its size and magnitude are not well understood yet. In this work, we analyze data from the nearest ground-based receivers of Global Navigation Satellite System (GNSS) to explore the ionospheric total electron content (TEC) response to this event. We show that the ionospheric response consists of a giant TEC increase followed by a strong long-lasting depletion. We observe that the explosive event of 15 January 2022 began at 04:05:54UT and consisted of at least 5 explosions. Based on the ionospheric TEC data, we estimate the energy released during the main major explosion to be between 9 and 37 Megatons in TNT equivalent. This is the first detailed analysis of the eruption sequence scenario and the timeline from ionospheric TEC observations.

Plain Language Summary

On 15 January 2022, the giant explosion of the Hunga Tonga-Hunga Ha'apai volcano shook the atmosphere of the Earth and generated a tsunami. The exact mechanism and timing of the eruption are not well understood yet, nor is the series of events that occurred directly following the first event. Many scientists are trying to understand the chronology of the eruption using different types of data. Here we investigate the signature of the eruption as recorded in Earth's ionosphere, the electrically conductive layer of the atmosphere from about 85-800 km of altitude. We observe variations in the total electron content (TEC) of the ionosphere using Global Navigation Satellite System (GNSS) receivers (commonly known as GPS receivers). Variations in the TEC through time

and space are caused by sound waves from the eruption traveling through the ionosphere. We use these variations to constrain the timing of the eruptive events, identifying at least five major explosions during this eruption. In addition, we use the amplitude of TEC variations to estimate that the largest explosion released energy of about 9 to 37 Megaton in trinitrotoluene (TNT) equivalent. This is the first detailed analysis of the eruption scenario and the timeline from ionospheric TEC observations.

Introduction

It is known that volcanic eruptions and explosions generate acoustic and gravity waves that reach the ionosphere and generate so-called co-volcanic ionospheric disturbances (CVIDs; e.g., Astafyeva, 2019; Meng et al., 2019). The ionospheric disturbances are usually registered about 10 to 45 minutes after the eruption onset and are observed directly above the volcano to as far away as 800-1000 km (Heki, 2006; Dautermann et al., 2009; Nakashima et al., 2014; Shults et al., 2016; Manta et al., 2021). CVID often represent quasi-periodic variations of ionospheric electron density or of total electron content (TEC) with periods of 12-30 min (e.g., Dautermann et al., 2009; Shults et al., 2016). The apparent velocity of propagation can vary between 550 m/s and 1100 km/s, which corresponds to gravito-acoustic, acoustic and shock-acoustic waves.

On January 15, 2022, a giant surtseyan volcanic explosion occurred at the uninhabited volcanic island Hunga Tonga-Hunga Ha'apai (HHTH) in South Pacific. The eruption caused the collapse of two-thirds of the volcanic edifice as reported from Sentinel 1 observations (<https://marine.copernicus.eu/news/satellites-observe-tsunami-triggered-tonga-volcano>), and triggered a tsunami. The interaction between the hot magma and sea water generated a large plume of ash and steam that reached as high as 33-35 km of altitude (e.g., Witze, 2022), and triggered giant atmospheric shock wave that propagated around the world several times (Duncombe, 2022). The eruption also generated large ionospheric disturbances that propagated around the world (Themens et al., 2022; Zhang et al., 2022).

The exact mechanism of the HTHH explosive eruption remains unknown, and the big scientific puzzle is complicated by the fact that the volcano is a submarine and ground-based instruments are not available nearby. Even the eruption onset time is still under debate. Observations from Himawari-8 satellite suggest that the eruption began sometime between 4:00 and 4:10 UT (Gusman and Rodger, 2022). The US Geological Survey (USGS), based on techniques calibrated for earthquakes, estimated that the eruption was equal to a M5.8 earthquake that began at 04:14:45UT (<https://earthquake.usgs.gov/earthquakes/eventpage/pt22015050/executive>). Poli & Shapiro (2022) based on analysis of long-period surface waves registered by seismic stations, calculated the onset at 04h16m00.07UT. Backprojection of surface pressure data in Tonga estimates the source time at 04:28±02 UT (Wright et al., 2022).

Here we study the ionospheric response to the HTHH explosion and, for the first time, we reconstruct the timeline of the HTHH eruption sequence fully based on ionospheric observations.

Data and methods

Global Navigation Satellite Systems (GNSS) are nowadays widely used for ionosphere sounding. Phase measurements from dual-frequency GNSS receivers allow to estimate the ionospheric TEC, which is an integrated value equal to the number of electrons along a line-of-sight (LOS) between a satellite and a receiver:

$$sTEC_{ph} = \frac{1}{A} \cdot \frac{f_1^2 f_2^2}{f_1^2 - f_2^2} (L_1 \lambda_1 - L_2 \lambda_2) \quad (1)$$

where $A = 40.308 \text{ m}^3/\text{s}^2$, L_1 and L_2 are phase measurements, and λ_1 and λ_2 are wavelengths at two GNSS frequencies. For the Global Positioning System (GPS) signals these are: $\lambda_1=1575,42$ and $\lambda_2=1227,60$ MHz). Most of GNSS (e.g., GPS, Galileo, BeiDou, QZSS) have fixed carrier frequencies. Whereas, in GLONASS each satellite has its own set of frequencies (e.g., Hofmann-Wellenhof et al., 2018; Shults et al., 2016).

In this study, the first data point is subtracted from the whole data series to remove an unknown bias that is always present in the phase measurements., i.e. we are analyzing relative TEC. Further, in order to remove the strong TEC dependence on a LOS elevation angle, we convert the slant TEC to vertical TEC by using the single-layer mapping function (Schaer et al., 1995). The TEC data are displayed in TEC units (TECU), with 1 TECU equal to 10^{16} electrons/ m^2 .

The spatial positions of ionospheric disturbances are calculated from so-called subionospheric points (SIPs), which are the projections of the intersection points between the LOS and the ionospheric thin shell at a fixed altitude that is often referred to as the altitude of detection *Hion*. Here we take $Hion = 320$ km, which is close to the maximum ionization height $HmF2$ as derived from the nearest ionosonde station NIUE located at 190.07E; 19.07S (<https://lgdc.uml.edu/common/DIDBMonthListForYearAndStation?ursiCode=ND61R&year=2022>).

In this study, we analyze non-filtered TEC data, in order to keep the amplitude of the signal and temporal characteristics unchanged. This also enables to better investigate the link between the eruption features and the ionospheric response. We use 30-sec data.

Results & Discussion

During the eruption, 15 ground-based GNSS-receivers were operational within ~ 2000 km distance from the volcano (Figure 1a). Most of these receivers captured signals from GPS (code “G”), GLONASS (code “R”), Galileo (code “E”), Beidou (code “C”), SBAS (code “S”) and QZSS (code “J”) satellite constellations. The following satellites showed clear CVID signatures in the ionospheric TEC data: G10, G18, G23, G24, G32, R07, R20, R21, E03, E36, C01, C04, C23, C24, C25, C27, C28, S33 (Figure 1b). In addition, a few stations captured signals from J01, J02, J03, J04 and J07 satellites. Such an impressive number of observation points allowed us to analyze the CVID evolution with an unprecedented level of detail.

1. TEC variations of unprecedented amplitude due to shock waves

The ionospheric TEC data series registered near the volcano are presented in Figure 1(c-f). The first CVID signatures are visible at ~ 4.45 UT, while several other large variations are seen at later

times. Interestingly, these TEC variations do not represent the “classic” quasi—periodic waveform observed in previous studies. These CVID are complex waveforms with a clear occurrence of N-waves with very sharp TEC increases, which is an indication of an acoustic or shock-acoustic wave source. Similar disturbances were observed following the giant M9 March 2011 Tohoku-Oki earthquake (e.g., Astafyeva et al., 2011; Liu et al., 2011).

The other remarkable observation is the amplitude of the TEC response to the HTHH eruption that reaches the extraordinary level of 5-8 TECU (Figure 1c-1f). Given the absolute background vertical TEC around the volcano varies from 18 to 23 TECU at the beginning of the eruption, we conclude that the CVID contribution to the background TEC is 21-44 %. This value is unprecedented with respect to previous studies that showed ~8% for eruptions with volcanic explosivity index (VEI) of 2, and 15-18% for VEI=4 eruptions (Shults et al., 2016).

2. Multiple volcanic explosions are detected by the ionosphere

We note that the TEC variations show multiple large peaks occurring between 4.45 and 5.6 UT (Figure 1c-f and Figure 2a). We propose that these individual peaks represent individual explosions that occurred between 4 and ~5UT (Figure 2b). The acoustic or shock-acoustic nature of the observed peaks can be confirmed from the N-type waveforms of the CVID and their apparent velocities (Figure S2). A similar complex TEC response was observed for the largest M9 earthquakes, driven by multiple rupturing segments of the megathrust fault: the 2011 Tohoku-Oki (Astafyeva et al., 2013b) and the 2004 Sumatra earthquake (Heki et al., 2006).

The scenario of multiple explosions is in line with conclusions by Wright et al. (2022) made from the analysis of surface pressure data recorded at a station in Tonga, only 64 km away from the HTHH volcano. Wright et al. (2022) identified the first peak at 04:26UT and four other events at 04:36UT, 05:10UT, 05:51UT and 08:46UT.

From the ionosphere, we can estimate the onset time by approximating CVID propagation as a spherical wave at a constant speed from a point source (Figure S1a; Kiryushkin and Afraimovich, 2007). Shults et al. (2016) used such an approximation to locate the eruptive source position fully based on ionospheric data. Here, we modify the previous algorithm by fixing the source at the volcano position and by only varying the CVID radial speed in order to obtain the most probable onset time (Text S1). From TEC data, we select peaks with clear N-wave-like waveforms that could represent explosions. For each event, we determine the CVID arrival times at the moment when the TEC starts to increase suddenly (Figure S1b), and the coordinates of the CVID detection (Tables S1,S2,S3,S4,S5). From these data and by applying our method, we obtain the following onset times for the five sub-events/explosions (Figure 2a): event #1 that lead to the preparation of the big explosions and the caldera collapse, began at 04:08:43UT. The largest two explosions occurred at 04:20:00 UT and at 04:28:05UT, then smaller sub-events took place at 04:48:30UT (#4) and at 04:55:21 UT (#5) (Table 1). We note that other TEC peaks were analyzed but did not give a solution. We therefore consider that they are not of acoustic nature.

To confirm these proposed event times and multiple events scenario, we model individual explosive events using the IonoSeis package (Rolland et al., 2013, Mikesell et al., 2019). This model uses one-dimensional sound speed and density profiles (Figure 3a, 3b, respectively) based on the local date and time computed with NRLMSIS 2.0 (Emmert et al., 2020). The model uses a three-

dimensional background electron density profile based on local date and time (IRI2016, Bilitza et al., 2017), as well as the local magnetic field inclination and declination (IGRF, Thébault et al., 2015). IonoSeis propagates an acoustic N-shaped pulse through the atmosphere from the location of the volcano at the Earth's surface to the ionosphere (Dessa et al., 2005). The neutral atmospheric wave is coupled into the ionosphere model and the slant TEC variation between satellite-receiver is computed (Mikesell et al., 2019). More details about the parameters chosen in this study can be found in Text S2 (Supplementary Material).

To reproduce the TEC series observed after the HTHH volcano explosion, five pulses of different amplitude were launched at different moments of time (Figure 3c). The modelling results confirm the occurrence of at least 5 explosions and also that events #2 and #3 were the largest. The simulations also provide us with another set of the onset times: the initial explosion (trigger) at 04:03:15UT, the main big explosion at 04:16:20UT, another big one at 04:24:45UT, and events #4 and #5 at 04:24:45UT and 05:02:15UT, respectively. The IonoSeis onsets are always 3.5-4.5 min ahead of those estimated by the spherical approximation method (Table 1), which can be explained by the difference in the approaches (constant velocity in the first method and a 1D velocity varying with altitude in the IonoSeis). Also, the spherical wave method is based on the manual determination of the arrival time, which can introduce additional inaccuracy. Knowing that IonoSeis tends to systematically delay the arrival of disturbance with respect to observations (Lee et al., 2018; Mikesell et al., 2019; Zedek et al., 2021), we provide the final ionospheric solution for the onset times by averaging the solutions by two ionospheric methods (Table 1). We obtain $04:05:54 \pm 169$ s UT for the onset HTHH eruption trigger event and $04:18:10 \pm 110$ UT for the main big explosion.

3. Explosion energy release as estimated from the ionosphere

From the ionospheric GNSS-derived TEC data it is possible to estimate the energy of the volcanic explosion (Heki, 2006; Dautermann et al, 2009). Heki (2006) suggested an empirical method based on analysis of CVID amplitudes with respect to the background TEC and comparison of the TEC response to Wyoming mine blasts of known explosive power by Calais et al. (1998). In that latter case, the explosion power of 1,5 kiloton in TNT equivalent generated TEC disturbance with the maximum amplitude of 0.03 TECU on the background absolute VTEC of 10.6 TECU. By using this method, Heki (2006) estimated the energy of the VEI=2 Asama volcano explosion as of $\sim 4 \times 10^4$ t TNT or 2×10^{14} Joule. However, it is important to note that besides the background TEC, other two factors affect the amplitude of CVID: the magnetic field configuration and the angle between the LOS and the disturbance wavefront (Otsuka et al., 2006; Kakinami et al., 2013; Rolland et al., 2013; Bagiya et al., 2019). Therefore, these parameters should be taken into account when comparing the disturbance amplitudes on the day of the Wyoming blast and the HTHH explosion.

In our case, multiple LOS on the north-west and north-east from the volcano detect CVID with similar amplitudes of 5-8 TECU, therefore, we conclude that the impact of the LOS-wavefront intersection is less important for such a huge event. Therefore, the rough estimation of the energy release is estimated by taking the maximum CVID amplitudes 5 and 8 TECU (at *samo-E03*, *usp1-G24*, *ftna-G24*, *ftna-E36*, *samo-R20*), and the background TEC (between 18 and 23 TECU). Knowing that the wave energy scales with the square of the amplitude, we estimate that the HTHH explosion is about 5900 and 24700 times more powerful than the mine blasts studied by Calais et al. (1998).

Therefore, the HTHH explosion power is between ~ 9 and 37 megaton (Mt) in TNT equivalent, or between $\sim 3.7 \times 10^{16}$ and 1.5×10^{17} J. This value is in agreement with estimations from other instruments and methods between 4 and 18 Mt of TNT (Garvin, 2022), and it is of the order of the 1883 Krakatoa volcano explosion, for which the acoustic energy was estimated as high as 8.6×10^{16} J (Woulff and McGretchun, 1976). The fact that the HTHH explosion generated a huge Lamb wave that travelled around the world at least 3 times (e.g., Zhang et al., 2022) is additional indication of the similar energy release with the Krakatoa explosion.

4. The giant and long-lasting ionospheric hole

In Figures 1c-1f, we notice an abrupt decrease in TEC starting from ~ 4.7 UT. This decrease is clearly observed by comparing the event data series to four quiet days preceding the eruption (10 to 13 January 2022) and the day after (Figure 4). Although we see day-to-day variations, the depletion is only present on 15 January. This ionospheric depletion (“hole”) resembles TEC response to the Tohoku-Oki earthquake and several other large earthquakes (e.g., Kakinami et al., 2012; Astafyeva et al., 2013a). Astafyeva et al. (2013a) demonstrated that the magnitude and the duration of the depletion scales with the magnitude of an earthquake and explained the hole as the rarefaction phase of the shock-acoustic wave. For the 2011 Tohoku-Oki earthquake, the depletion lasted 30-50 min and the TEC decreased by -5 to -6 TECU with respect to the before-earthquake level (Astafyeva et al., 2013a,b). In the case of the HTHH event, the depletion of the amplitude of -13-18 TECU lasted for at least 1.5-2 hours (Figure 4), which is unprecedented, both in magnitude and duration. This could be explained, first of all, by the fact that eruptive explosions should generate stronger shock waves than earthquakes because the source is located at shallow depth (about 200 m) under water but not underground. The giant shock wave would cause large-amplitude and long-lasting rarefaction phase. Similarly, Aa et al. (2022) suggested that the depletion was composed of cascading TEC decreases due to different acoustic wave impulses.

Second, it is possible that the HTHH ionospheric depletion was reinforced by a geomagnetic storm that began several hours before the eruption, and was in an early recovery phase at the time of the CVID observations. While the storm was moderate (minimum Dst excursion of -100 nT, World Data Center for Geomagnetism, 2015), the storm-time composition changes were significant, as the data of the Global Ultraviolet Imager (GUVI) onboard the Thermosphere, Ionosphere, Mesosphere Energetics and Dynamics (TIMED) satellite (<http://guvitimed.jhuapl.edu/>, Christensen et al., 2003) show (Figure S3). The O/N2 ratio was reduced above the area of the CVID observations, which means decreased ionization (e.g., Prölss, 1976).

Third, unlike the Tohoku-Oki earthquake that occurred in the local afternoon, the HTHH depletion developed during local evening hours, which undoubtedly also have played a role in the retarded recovery from the hole because of the decreased evening ionization level.

The extremely low local ionization level due to the depletion made it difficult to clearly detect and to analyze one later eruption that took place around 8:30UT (Figure S4; Wright et al., 2022).

Conclusions

The extraordinary Hunga Tonga-Hunga Ha’apai volcano eruption and related explosive events generated quite significant and long-lasting effects in the ionosphere. Shortly after the eruption onset, GNSS-receivers around the volcano area showed TEC variations with several distinct peaks

that correspond, most likely, to a trigger event (the initial explosion) at 04:05:54±169s UT and 4 other explosions that occurred between 4:18 and 4:54UT on 15 January 2022.

The second and the most powerful explosion occurred at 04:18:10UT. Based on the CVID amplitudes and the background TEC value, we estimate that this major explosion released energy between 9 and 37 Megaton in TNT equivalent, that is comparable to the 1883 Krakatoa event.

The large TEC increase was followed by major depletion in the ionosphere in the vicinity of the volcano. The TEC dropped by -13 to -18 TECU below the quiet TEC values, and the depletion lasted for at least 1,5-2 hours, which is unprecedented. The depletion was primarily caused by the giant shock waves, and represents the rarefaction phase of the giant CVID.

We demonstrate that numerous ionospheric sounding points in the vicinity of the volcano can help to decipher the eruption scenario and chronology. This is the first study of the kind.

Open Research

All GNSS data are available from the CDDIS archives [https://cddis.nasa.gov/Data and Derived Products/GNSS/daily 30second data.html](https://cddis.nasa.gov/Data_and_Derived_Products/GNSS/daily_30second_data.html) and data of RAUL station are from the Geological hazard information for New Zealand (GeoNet) database via <https://data.geonet.org.nz/gnss/rinex/2022/015/>. The thermospheric O/N2 composition data are available from: <http://guvitimed.jhuapl.edu/guvi-galleryl3on2>. The TEC estimation “tec-suite” codes are accessible from <https://tec-suite.readthedocs.io/en/latest/installation.html>. The GMT6.0 software is available at <https://www.generic-mapping-tools.org/download/>.

Acknowledgement

This work was supported by the French Space Agency (CNES), projects “RealDetect” (EA, BM) and “UV-TECGEOX” (LR, EM). LR, EM and TDM acknowledge the support of the French National Agency of Research (ANR), project ITEC (grant ANR-19-CE04-0003), and project Université Côte d’Azur Investissement d’Avenir Idex. MR, EM and MB thank the CNES for the PhD and PostDoctoral Fellowships. We thank I. Zhivetiev for the “tec-suite” codes. Figures were done by using the GMT6.0 software (Wessel et al., 2019).

References

- Aa, E., S.-R. Zhang, et al. (2022) Significant equatorial plasma bubbles and global ionospheric disturbances after the 2022 Tonga volcano eruption, *ESSOAr*, Doi: 10.1002/essoar.10510637.1, <https://www.essoar.org/doi/abs/10.1002/essoar.10510637.1>
- Astafyeva, E. (2019) Ionospheric detection of natural hazards. *Reviews of Geophysics*, **57(4)**, 1265-1288. <https://doi.org/10.1029/2019RG000668>.
- Astafyeva, E., P. Lognonné, L. Rolland (2011), First ionosphere images for the seismic slip on the example of the Tohoku-Oki earthquake. *Geophys. Res. Lett.*, V.38, L22104, DOI:10.1029/2011GL049623.

302 Astafyeva, E., S. Shalimov, E. Olshanskaya, P. Lognonné (2013a) Ionospheric response to
 303 earthquakes of different magnitudes: larger quakes perturb the ionosphere stronger and
 304 longer. *Geophys. Res. Lett.*, V.40, N9, 1675-1681, DOI: 10.1002/grl.50398.
 305 Astafyeva, E., L. Rolland, P. Lognonné, K. Khelifi, T. Yahagi. (2013b) Parameters of seismic source as
 306 deduced from 1Hz ionospheric GPS data: case-study of the 2011 Tohoku-Oki event. *J. Geophys.*
 307 *Res.*, V. 118, 9, 5942-5950. DOI:10.1002/jgra50556.
 308 Bagiya et al. (2019) Mapping the Impact of Non-Tectonic Forcing mechanisms on GNSS measured
 309 Coseismic Ionospheric Perturbations. *Sci. Reports.* 9:18640, doi:10.1038/s41598-019-54354-0.
 310 Bilitza, D., Altadill, D., Truhlik, V., Shubin, V., Galkin, I., Reinisch, B., & Huang, X. (2017). International
 311 Reference Ionosphere 2016: From ionospheric climate to real-time weather predictions. *Space*
 312 *Weather*, 15, 418–429. <https://doi.org/10.1002/2016SW001593>
 313 Calais, E., J. B. Minster, M. A. Hofton, and H. Hedlin (1998), Ionospheric signature of surface mine
 314 blasts from Global Positioning System measurements, *Geophys. J. Int.*, 132, 191– 202.
 315 Christensen, A. B., et al. (2003), Initial observations with the Global Ultraviolet Imager (GUVI) on
 316 the NASA TIMED satellite mission, *J. Geophys. Res.*, 108(A12), 1451,
 317 doi:10.1029/2003JA009918.
 318 Dautermann, T., E. Calais, and G. S. Mattioli (2009), Global Positioning System detection and energy
 319 estimation of the ionospheric wave caused by the 13 July 2003 explosion of the Soufrière Hills
 320 Volcano, Montserrat, *J. Geophys. Res.*, 114, B02202, doi:10.1029/2008JB005722.
 321 Dessa, J. X., Virieux, J., & Lambotte, S. (2005). Infrasound modeling in a spherical heterogeneous
 322 atmosphere. *Geophysical Research Letters*, 32(12), 1–5.
 323 <https://doi.org/10.1029/2005GL022867>
 324 Duncombe, J. (2022), The surprising reach of Tonga's giant atmospheric waves, *Eos*,
 325 103, <https://doi.org/10.1029/2022EO220050>. Published on 21 January 2022.
 326 Emmert, J. T., Drob, D. P., Picone, J. M., Siskind, D. E., Jones, M. Jr., Mlynczak, M. G., et al. (2020).
 327 NRLMSIS 2.0: A whole-atmosphere empirical model of temperature and neutral species
 328 densities. *Earth and Space Science*, 7, e2020EA001321. <https://doi.org/10.1029/2020EA001321>
 329 Fuller-Rowell, T. J., Codrescu, M. V., Moffett, R. J., & Quegan, S. (1994). Response of the
 330 thermosphere and ionosphere to geomagnetic storms. *Journal of Geophysical Research*, 99(A3),
 331 3893–3914. <https://doi.org/10.1029/93JA02015>
 332 Garvin, J. (2022). Dramatic Changes at Hunga Tonga-Hunga Ha'apai. Available at:
 333 [https://earthobservatory.nasa.gov/images/149367/dramatic-changes-at-hungatonga-hunga-](https://earthobservatory.nasa.gov/images/149367/dramatic-changes-at-hungatonga-hunga-haapai)
 334 [haapai](https://earthobservatory.nasa.gov/images/149367/dramatic-changes-at-hungatonga-hunga-haapai)
 335 Gusman, A.R. & Roger, J. (2022). Hunga Tonga - Hunga Ha'apai volcano-induced sea level oscillations
 336 and tsunami simulations. GNS Science webpage, <https://doi.org/10.21420/DYKJ-RK41>
 337 Heki, K. (2006), Explosion energy of the 2004 eruption of the Asama Volcano, central Japan, inferred
 338 from ionospheric disturbances, *Geophys. Res. Lett.*, 33, L14303, doi:10.1029/2006GL026249.
 339 Heki, K., Y. Otsuka, N. Choosakul, N. Hemmakorn, T. Komolmis, and T. Maruyama (2006), Detection
 340 of ruptures of Andaman fault segments in the 2004 great Sumatra earthquake with coseismic
 341 ionospheric disturbances, *J. Geophys. Res.*, 111, B09313, doi:10.1029/2005JB004202.
 342 Hofmann-Wellenhof, B., H. Lichtenegger & E. Wasle. (2008) GNSS-Global Navigation Satellite
 343 Systems. *Springer, Vienna*, <https://doi.org/10.1007/978-3-211-73017-1>

344 Kakinami, Y. et al. (2012) Tsunamigenic ionospheric hole, *Geophys. Res. Lett.*, 39, L00G27,
345 doi:10.1029/2011GL050159.

346 Kakinami et al. (2013), Ionospheric ripples excited by superimposed wave fronts associated with
347 Rayleigh waves in the thermosphere, *J. Geophys. Res.*, doi:10.1002/jgra.50099.

348 Kiryushkin, V.V. and E.L. Afraimovich (2007) Determining the Parameters of Ionospheric
349 Perturbation Caused by Earthquakes Using the Quasi-Optimum Algorithm of Spatiotemporal
350 Processing of TEC Measurements, *Earth Planets Space*, 2007, vol. 59, pp. 267–278.

351 Lee, R. F., Rolland, L. M., & Mikesell, T. D. (2018). Seismo-Ionospheric Observations, Modeling, and
352 Backprojection of the 2016 Kaikōura Earthquake. *Bulletin of the Seismological Society of*
353 *America*, 108(3B), 1794–1806. <https://doi.org/10.1785/0120170299>

354 Manta, F., G. Occhipinti, E. Hill, A. Perttu, B. Taisne (2021) Correlation Between GNSS-TEC and
355 Eruption Magnitude Supports the Use of Ionospheric Sensing to Complement Volcanic Hazard
356 Assessment, *J. Geophys. Res. - Solid Earth*, doi:10.1029/2020JB020726

357 Meng, X., Vergados, P., Komjathy, A., & Verkhoglyadova, O. (2019) Upper atmospheric responses to
358 surface disturbances: An observational perspective. *Radio Science* **54**, 1076 – 1098.
359 <https://doi.org/10.1029/2019RS006858>

360 Mikesell, T.D.; Rolland, L.M.; Lee, R.F.; Zedek, F.; Coisson, P.; Dessa, J.-X. (2019) *IonoSeis*: A Package
361 to Model Coseismic Ionospheric Disturbances. *Atmosphere*, 10, 443.
362 <https://doi.org/10.3390/atmos10080443>

363 Nakashima, Y., K. Heki, A. Takeo, M.N. Cahyadi, A. Aditiya, K. Yoshizawa. (2016) Atmospheric
364 resonant oscillations by the 2014 eruption of the Kelud volcano, Indonesia, observed with the
365 ionospheric total electron contents and seismic signals. *Earth and Planetary Science Letters*, V.
366 434, 112-116, doi:10.1016/j.epsl.2015.11.029.

367 Otsuka et al. (2006), GPS detection of total electron content variations over Indonesia and Thailand
368 following the 26 December 2004 earthquake, *Earth Planets Space*, 58, 159-165, doi:
369 10.1186/BF03353373.

370 Poli, P. and M. Shapiro (2022) Rapid characterization of large volcanic eruptions: measuring the
371 impulse of the Hunga Tonga explosion from teleseismic waves. *Geophys. Res. Letters*, V. 49,
372 e2022GL098123, doi: 10.1029/2022GL098123

373 Prölss, G. W. (1976) On explaining the negative phase of ionospheric storms, *Planet. Space Sci.*, 24,
374 607-609.

375 Rolland, L. M., M. Vergnolle, J.-M. Nocquet, A. Sladen, J.-X. Dessa, F. Tavakoli, H.R. Nankali, and F.
376 Cappa (2013), Discriminating the tectonic and non-tectonic contributions in the ionospheric
377 signature of the 2011, Mw7.1, dip-slip Van earthquake, Eastern Turkey, *Geophys. Res. Lett.*, 40,
378 doi:10.1002/grl.50544.

379 Schaer, S., G. Beutler, L. Mervart, M. Rothacher (1995) Global and regional ionosphere models using
380 the GPS double difference phase observable, *Proceedings of the 1995 IGS Workshop, Potsdam,*
381 *Germany, May 15–17, 1995.* <https://mediatum.ub.tum.de/doc/1365730/137709.pdf>

382 Shults, K., E. Astafyeva and S. Adourian (2016). Ionospheric detection and localization of volcano
383 eruptions on the example of the April 2015 Calbuco events. *J. Geophys. Res. -Space Physics*,
384 V.121, N10, 10,303-10,315, doi:10.1002/2016JA023382.

385 Thébault, E.; Finlay, C.C.; Beggan, C.D.; Alken, P.; Aubert, J.; Barrois, O.; Bertrand, F.; Bondar, T.;
386 Boness, A.; Brocco, L.; et al. Wardinski, I.; Zvereva, T. (2015) International Geomagnetic

387 Reference Field: The 12th generation. *Earth Planets Space*, 67, 79, doi:10.1186/s40623-015-
388 0228-9

389 Themens, D. R., Watson, C., Žagar, N., Vasylykevych, S., Elvidge, S., McCaffrey, A., et al. (2022). Global
390 propagation of ionospheric disturbances associated with the 2022 Tonga Volcanic Eruption.
391 *Geophysical Research Letters*, 49, e2022GL098158. doi.org: 10.1029/2022GL098158

392 Wessel, P., J.F. Luis, L. Uieda, R. Scharroo, F. Wobbe, W.H.F. Smith, D. Tian (2019) The Generic
393 Mapping Tools Version 6. *Geochemistry, Geophysics, Geosystems*. V. 20, N11, Doi:
394 10.1029/2019GC00851

395 Witze, A. (2022) Why the Tongan volcanic eruption was so shocking. *Nature*, Vol.602, p. 376-378.
396 doi: d41586-022-00394 [https://media.nature.com/original/magazine-assets/d41586-022-](https://media.nature.com/original/magazine-assets/d41586-022-00394-y/d41586-022-00394-y.pdf)
397 [00394-y/d41586-022-00394-y.pdf](https://media.nature.com/original/magazine-assets/d41586-022-00394-y/d41586-022-00394-y.pdf).

398 World Data Center for Geomagnetism, Kyoto, M. Nose, T. Iyemori, M. Sugiura, T. Kamei (2015),
399 Geomagnetic Dst index, http://wdc.kugi.kyoto-u.ac.jp/dst_realtime/202201/index.html, doi:
400 10.17593/14515-74000.

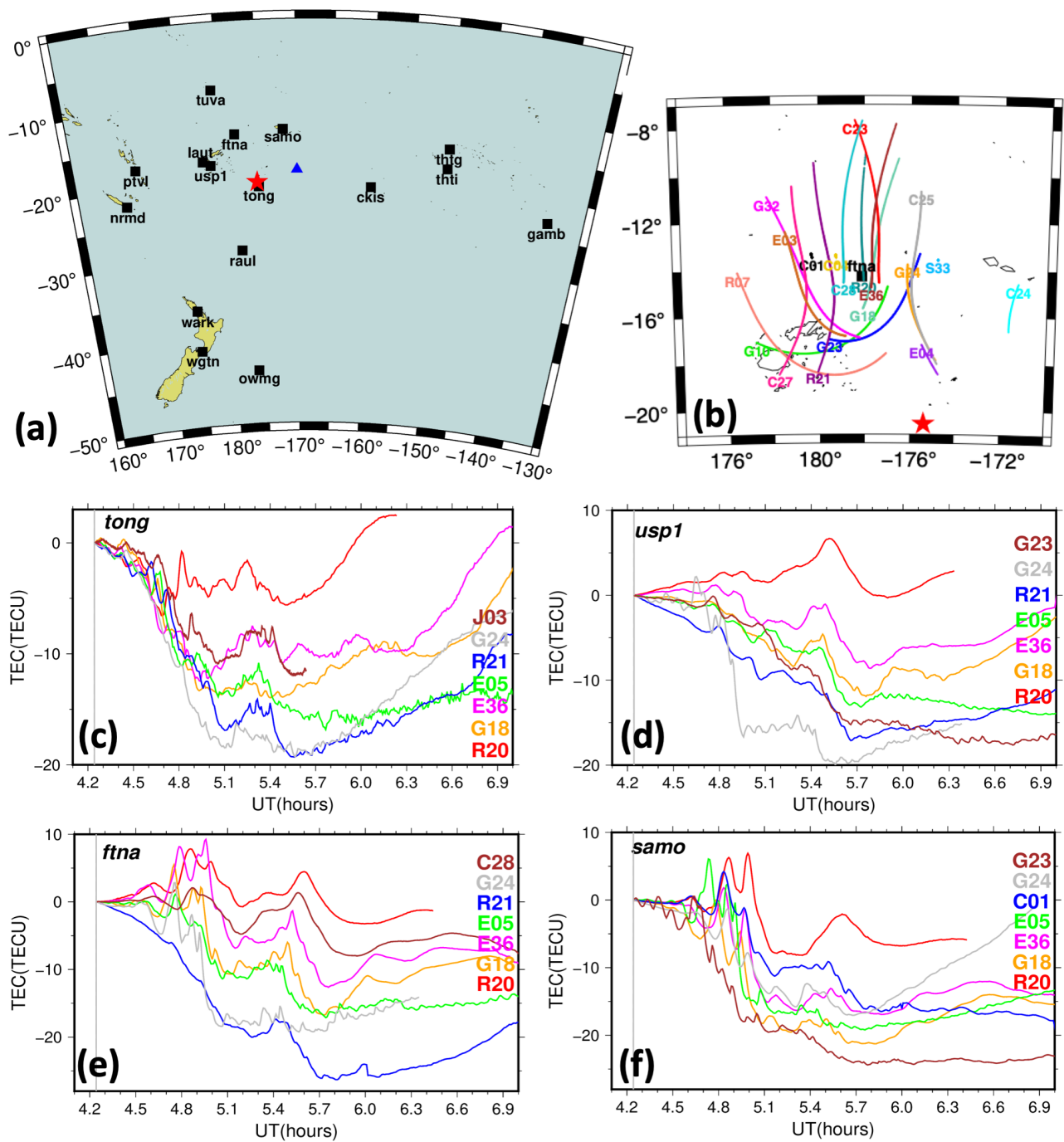
401 Wright, C.J., et al. (2022) Tonga eruption triggered waves propagating globally from surface to edge
402 of space, *ESSOAr*, <https://www.essoar.org/pdfs/10.1002/essoar.10510674.1>

403 Woulff, G., and T. R. McGetchin (1976), Acoustic noise from volcanoes—Theory and experiment,
404 *Geophys. J. R. Astron. Soc.*, 45, 601–616.

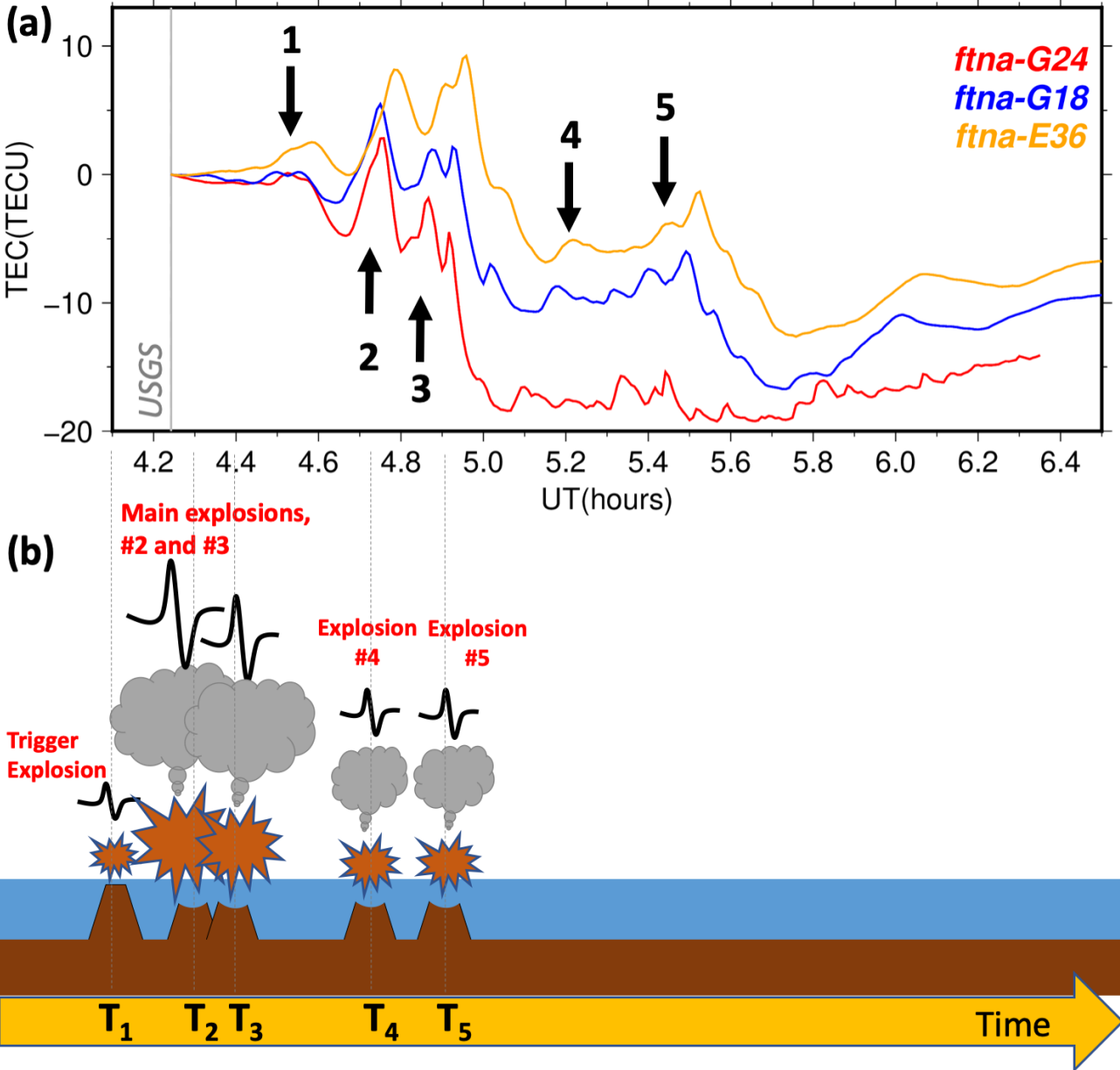
405 Zedek, F., Rolland, L. M., Mikesell, T. D., Sladen, A., Delouis, B., Twardzik, C., & Coïsson, P. (2021).
406 Locating surface deformation induced by earthquakes using GPS, GLONASS and Galileo
407 ionospheric sounding from a single station. *Advances in Space Research*, 68(8), 3403–3416.
408 <https://doi.org/10.1016/j.asr.2021.06.011>

409 Zhang S-R, Vierinen J, Aa E, Goncharenko LP, Erickson PJ, Rideout W, Coster AJ and Spicher A (2022)
410 2022 Tonga Volcanic Eruption Induced Global Propagation of Ionospheric Disturbances via
411 Lamb Waves. *Front. Astron. Space Sci.* 9:871275. doi: 10.3389/fspas.2022.871275.

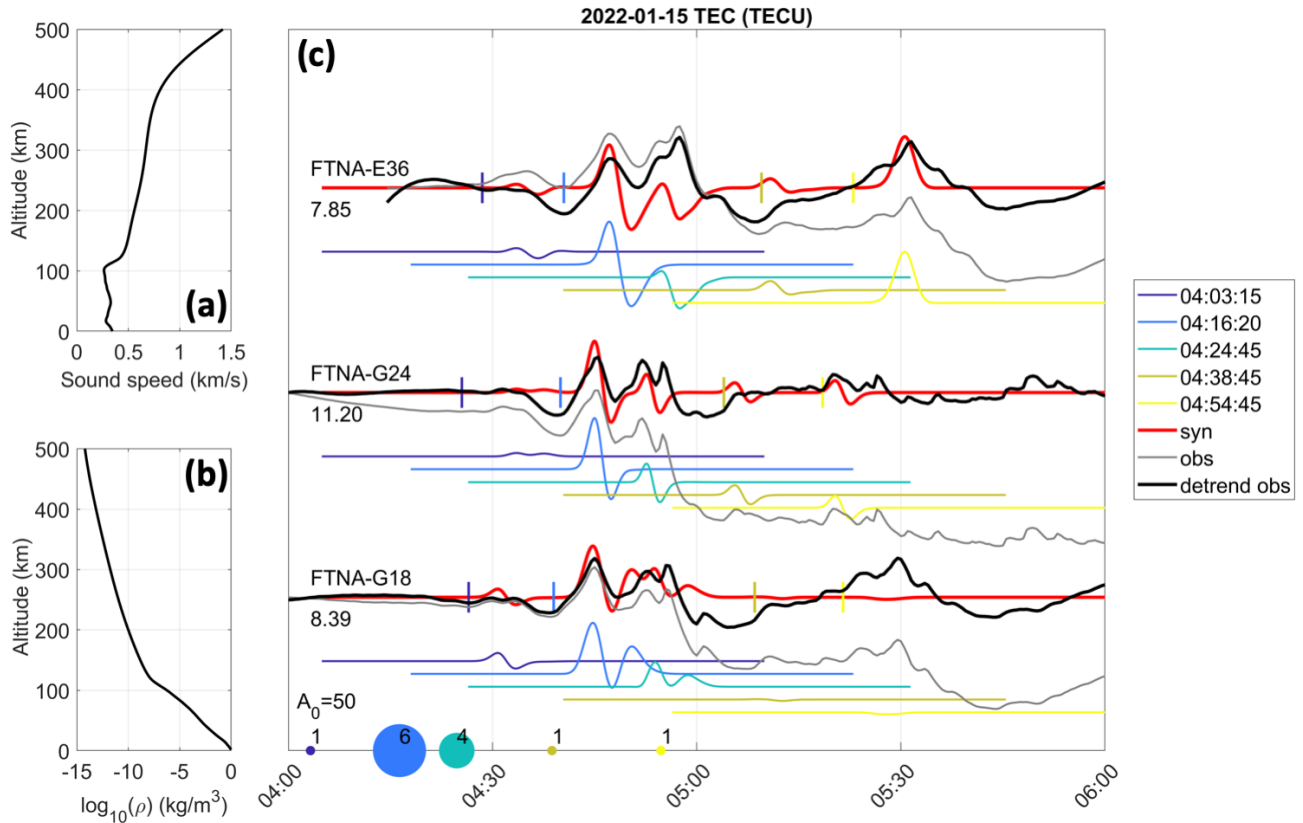
412 **Figure Captions**
 413 **Figure 1. (a)** The geometry of CVID observations by multiple GNSS. Black squares show the GNSS
 414 stations, the red star depicts the volcano (175.382W; 20.53S), blue triangle - the ionosonde station;
 415 **(b)** IPP trajectories for the station FTNA at the altitude $H_{ion}=320$ km, for the time period between
 416 4:14 (the USGS eruption time onset) and 8UT. Satellite names are shown at the beginning of each
 417 IPP trajectory that corresponds to the eruption onset; **(c-f)** Ionospheric TEC variations registered by
 418 the four closest GNSS receivers: *tong* (c), *usp1* (d), *ftna* (e) and *samo* (f). Names of satellites
 419 are noted on the panels.
 420



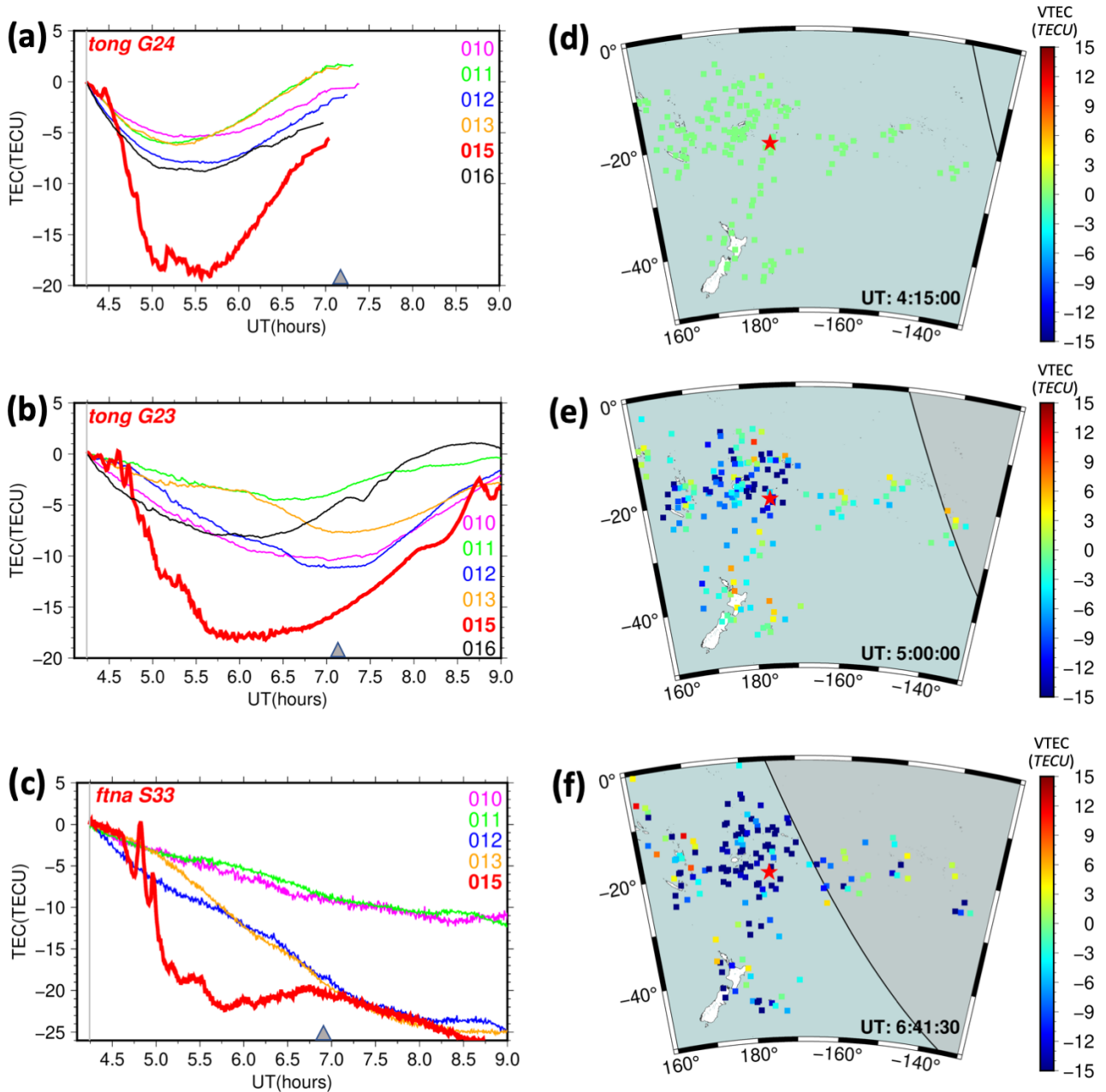
423 **Figure 2. (a)** Ionospheric disturbances corresponding to 5 explosions that most likely took place on
424 15 January 2022. Grey vertical line denotes the USGS onset time; **(b)** Suggested scenario and the
425 timeline of the HTHH volcano explosions of 15 January 2022. Each explosion emits an acoustic pulse
426 of different amplitude as illustrated. Vertical dotted lines correspond to the ionospherically-
427 determined onset times of the explosions.
428



438 **Figure 3. (a)** sound speed and **(b)** neutral density profiles used to model the TEC response by using
 439 IonoSeis software; **(c)** Comparison of slant TEC observations (gray and black curves) with IonoSeis
 440 simulations (red curves) for FTNA-E36, FTNA-G24, FTNA-G18 LOS. The black and grey slant TEC
 441 curves have been scaled by the coefficient indicated just above the receiver-satellite pair name. Thin
 442 colored curves show different pulses launched at different moments of time as shown on the legend
 443 on the right. The dots on the bottom x-axis indicate relative size of source based on a scalar
 444 amplitude factor. The numbers are relative to the first event, which has amplitude 1.



447 **Figure 4. (a-c)** Ionospheric depletion as seen on the eruption day (red curve, 015) with respect to
 448 four quiet days before (010, 011, 012, 013) and the day after the eruption (016) as recorded by *tong*
 449 station and *G24* satellite **(a)**, *tong G23* **(b)**, and *ftna S33* **(c)**. Gray triangles depict the approximate
 450 time of the solar terminator; **(d-f)** TEC snapshots plotted by using data of all satellites and all stations
 451 shown in Figures 1a-b: **(d)** close to the eruption onset at 04:15UT; **(e-f)** during the depletion
 452 observations at 05:00UT and 06:41UT.
 453



459 **Table 1:** Time onsets of the five HTHH volcano explosions as estimated from the ionosphere: by
 460 using the approximation of spherical wave at constant radial velocity (columns 4-5), $\text{Onset}_{\text{SPHER}}$, and
 461 by using the IonoSeis software, $\text{Onset}_{\text{IonoSeis}}$ (column 6). The final ionospheric onset time was
 462 calculated by averaging the solutions in columns 5 and 6.
 463

#	Sub-Event	CVID detection time (UT)	CVID radial Velocity (m/s)	$\text{Onset}_{\text{SPHER}}$ (UT)	$\text{Onset}_{\text{IonoSeis}}$ (UT)	$\text{Onset}_{\text{iono}}$ (UT \pm sec)
1	Trigger/initial event	04:20:00, 04:22:30	620	04:08:43	04:03:15	04:05:54 \pm 169
2	Main explosion	04:25:30; 04:28:00	620	04:20:00	04:16:20	04:18:10 \pm 110
3	Explosion 3	04:51:30; 04:53:00	510	04:28:05	04:24:45	04:26:25 \pm 100
4	Explosion 4	05:05:30; 05:07:30	770	04:48:30	04:38:45	04:43:37 \pm 292
5	Explosion 5	05:08:30; 05:15:30	550	04:55:21	04:54:45	04:54:27 \pm 18